

OPTICAL PROPERTIES OF AMORPHOUS ALUMINA DUST IN THE ENVELOPES AROUND O-RICH AGB STARS

KYUNG-WON SUH

Department of Astronomy and Space Science, Chungbuk National University, Cheongju 28644, Korea
kwsuh@chungbuk.ac.kr

Received June 22, 2016; accepted July 12, 2016

Abstract: We investigate optical properties of amorphous alumina (Al_2O_3) dust grains in the envelopes around O-rich asymptotic giant branch (AGB) stars considering the laboratory measured optical data. We derive the optical constants of amorphous alumina in a wide wavelength range that satisfy the Kramers-Kronig relation and reproduce the laboratory measured data. Using the amorphous alumina and silicate dust, we compare the radiative transfer model results with the observed spectral energy distributions. Comparing the theoretical models with the observations on various IR two-color diagrams for a large sample O-rich AGB stars, we find that the amorphous alumina dust (about 10-40 %) mixed with amorphous silicate can reproduce much more observed points for the O-rich AGB stars with thin dust envelopes.

Key words: stars: AGB and post-AGB – dust: extinction – circumstellar matter – infrared: stars – radiative transfer

1. INTRODUCTION

The main site of dust formation is believed to be the cool envelopes around asymptotic giant branch (AGB) stars. O-rich AGB stars (M-type Miras and OH/IR stars) typically show conspicuous $10\ \mu\text{m}$ and $18\ \mu\text{m}$ features in emission or absorption. They suggest the presence of amorphous silicate dust grains in the outer envelopes around them (Jones & Merrill 1976).

Low mass-loss rate O-rich AGB (LMOA) stars with thin dust envelopes show the $10\ \mu\text{m}$ and $18\ \mu\text{m}$ emission features of amorphous silicate. High mass-loss rate O-rich AGB (HMOA) stars with thick dust envelopes show the absorbing features at the same wavelengths (e.g., Suh 2004). Water-ice was found in some HMOA stars (Justtanont et al. 2006; Suh & Kwon 2013) and amorphous alumina (Al_2O_3) dust grains were detected in many LMOA stars (e.g., Sloan & Price 1998).

In a number of previous works (e.g., Markwick-Kemper et al. 2007; Suh & Kwon 2011), the term corundum was erroneously assigned to different kinds of solid alumina regardless of its crystal structure. However, only one of the crystalline Al_2O_3 polymorphs deserves the name corundum: namely $\alpha\text{-Al}_2\text{O}_3$ which has trigonal lattice symmetry (e.g., Koike et al. 1995). While the amorphous aluminum oxide material (Al_2O_3) synthesized by Begemann et al. (1997) shows a single peak at $11.8\ \mu\text{m}$, corundum shows much sharper multiple peaks around $12\ \mu\text{m}$ (Koike et al. 1995; Zeidler et al. 2013).

In this work, we investigate optical properties of amorphous alumina (Al_2O_3) dust in the envelopes around O-rich AGB stars. We derive the optical constants of the alumina dust in a wide wavelength range, which satisfy the Kramers-Kronig relation and repro-

duce the laboratory measured optical data. Using the opacity function of the amorphous alumina dust, we compare the theoretical radiative transfer model results with the observed spectral energy distributions (SEDs) and observations on various IR two-color diagrams (2CDs) for a large sample O-rich AGB stars.

2. AMORPHOUS ALUMINA DUST

Dust opacity is determined from the optical constants ($m_\lambda = n_\lambda + ik_\lambda$), shape, and size of a dust grain. The optical constants may be expressed by the complex index of refraction, $m = n + ik$, where $\varepsilon = m^2$. We can derive two functions of complex dielectric constants, $\varepsilon_1(\lambda)$ and $\varepsilon_2(\lambda)$, from the opacity function $Q_{ext}(\lambda)$ considering the required supplementary physical constraint. Namely, the dielectric constants should satisfy the Kramers-Kronig relation (e.g., Bohren & Huffman 1983).

Silicate dust is believed to be the main dust species for O-rich AGB stars (Jones & Merrill 1976; Suh 1999). Alumina dust has been detected in the spectra of many LMOA stars in our Galaxy (Sloan & Price 1998; Speck et al. 2000) and the Large Magellanic Cloud (Jones et al. 2014). The shape of the $10\ \mu\text{m}$ emission feature of LMOA stars, which is mainly produced by silicates, can be modified by addition of the alumina dust.

The broad $10\ \mu\text{m}$ emission feature in $\lambda = 8\text{--}15\ \mu\text{m}$ is best fitted with a mixture of amorphous alumina and silicate dust. Suh & Kwon (2011) found that the dust opacity using the alumina dust as well as silicates can improve the model fit on IR 2CDs for a large sample of LMOA stars. Egan & Sloan (2001) and Jones et al. (2014), who modeled the alumina abundance of O-rich AGB stars, found that the $10\ \mu\text{m}$ absorption feature is likely to be produced by only silicate dust for HMOA

stars.

Begemann et al. (1997; hereafter Be97) presented the optical constants for amorphous alumina (Al_2O_3) in the wavelength range 7.8–500 μm . The alumina grains produce a single peak at 11.8 μm and influences the shape of the SED at around 10 μm . The bulk density of the amorphous alumina is 3.2 g cm^{-3} .

Suh & Kwon (2011) and Jones et al. (2014) used the optical constants for amorphous (porous) alumina grains obtained by Be97 in the wavelength range 7.8–500 μm , which are extended to the shorter wavelength range ($\lambda < 7.8 \mu\text{m}$) by concatenation with the optical constants of corundum dust measured by Koike et al. (1995; hereafter Ko95). However, the interpolated optical constants are not physically reliable because they are from different materials and do not satisfy the Kramers-Kronig relation.

2.1. Deriving the optical constants

To obtain the complex dielectric functions, we have used the following procedure similar to that used in Suh (1999):

(i) $\varepsilon_2(\lambda)$ is adopted over a electromagnetic spectrum to agree with the existing laboratory data.

(ii) $\varepsilon_1(\lambda)$ is obtained using the Kramers-Kronig relation

$$\varepsilon_1(\lambda) = 1 + \frac{2}{\pi} P \int_0^{\infty} \frac{x \varepsilon_2(x)}{x^2 - \lambda^2} dx \quad (1)$$

where P indicates the Cauchy principal value.

(iii) From the complex dielectric function, we calculate $\kappa_{abs}(\lambda)$. $\kappa_{abs}(\lambda)$ is compared with the desired opacity function.

(iv) Where disagreements is found, the choice of $\varepsilon_2(\lambda)$ is modified, and steps (ii) - (iv) are repeated.

From the satisfactory sets of complex dielectric constants, we can calculate the optical constants ($m(\lambda) = n + ik$).

2.2. Models for amorphous alumina dust

Figure 1 shows the opacity function (mass absorption coefficients) and complex dielectric constants for three different models of alumina dust. The opacity function of amorphous warm silicate (Suh 1999) is also displayed for comparison. Using the Mie theory (Bohren & Huffman 1983), the opacity functions are calculated for spherical dust grains whose uniform radius is 0.1 μm . The opacity function for amorphous (porous) alumina dust measured by Be97 shows a single peak at 11.8 μm .

For model 1, we have derived the sets of complex dielectric constants in the wavelength range 0.1–3600 μm using the Kramers-Kronig procedures described in section 2.1. We use the same $\varepsilon_2(\lambda)$ in the wavelength range 7.8–500 μm as presented by Be97 for amorphous (porous) alumina (Al_2O_3). In other wavelength ranges, we have derived $\varepsilon_2(\lambda)$ so that the calculated $\varepsilon_1(\lambda)$ in the wavelength range 7.8–500 μm is almost the same as the one presented by Be97. Small deviations of $\varepsilon_1(\lambda)$ around the end points (7.8 and 500 μm) were not avoidable. In the shorter (0.1–7.8 μm) wavelength range, where the

Table 1
Models for amorphous alumina dust

Model	Laboratory Data ¹	K-K ²	Usage ¹
model 1	Be97	Yes	This work
model 2	Be97; Ko95	Yes	-
model 3	Be97; Ko95	No	SK11; Jon14

¹Be97: Begemann et al. (1997); Ko95: Koike et al. (1995); SK11: Suh & Kwon (2011); Jon14: Jones et al (2014), ²K-K: the Kramers-Kronig relation.

laboratory data are not available, the opacity function is similar to that of silicate dust. In the longer (500–3600 μm) wavelength range, where the laboratory data are not available, the opacity function obeys approximately a simple power law ($\kappa_{abs} \propto \lambda^{-2}$) just like silicate dust.

For model 2, we use $\varepsilon_2(\lambda)$ from Be97 (amorphous porous alumina) in the wavelength range 7.8–500 μm and from Ko95 (corundum) in the shorter wavelength range ($\lambda < 7.8 \mu\text{m}$). $\varepsilon_1(\lambda)$ is calculated from the combined $\varepsilon_2(\lambda)$ using the Kramers-Kronig relation. Because of the small change of $\varepsilon_2(\lambda)$ from model 1 in $\lambda < 7.8 \mu\text{m}$ (see the lower panel of Figure 1), the calculated $\varepsilon_1(\lambda)$ and opacity function for model 2 in the wavelength range 7.8–500 μm are very different from those for model 1 (or Be97). Model 2 would not be physically reliable because the complex dielectric constants are from different materials.

For model 3, the optical constants (n and k) for amorphous (porous) alumina grains obtained by Be97 are extended to the shorter wavelength range ($\lambda < 7.8 \mu\text{m}$) by concatenation with the optical constants of corundum measured by Ko95. $\varepsilon_2(\lambda)$ is the same as the one from Ko95, but $\varepsilon_1(\lambda)$ shows some deviations in the range $\lambda < 7.8 \mu\text{m}$ (see Figure 1) because of differences in the two sets of optical constants (Be97 and Ko95) at 7.8 μm . Compared with model 2, model 3 shows the same $\varepsilon_2(\lambda)$ but different $\varepsilon_1(\lambda)$. This model was used by Suh & Kwon (2011) and Jones et al. (2014). Because the interpolated optical constants are from different materials and do not satisfy the Kramers-Kronig relation, model 3 would not be physically reliable.

Table 1 summarizes properties of the three models. Even though the three models can reproduce the observations in similar ways, it is meaningless to use physically unreliable models for amorphous alumina because other dust species could also produce similar features in the wavelength range. Therefore, we use only model 1 for amorphous alumina dust in this work.

3. RADIATIVE TRANSFER MODEL CALCULATIONS

We use the radiative transfer code DUSTY developed by Ivezić & Elitzur (1997) for a spherically symmetric dust shell. We have performed the model calculations in the wavelength range 0.1 to 3600 μm . For all models, we assume the dust density distribution is continuous ($\rho \propto r^{-2}$). The dust condensation temperature (T_c) is assumed to be 400-1000 K. The outer radius of the dust shell is always taken to be 10^4 times the inner radius (R_c). We choose 10 μm as the fiducial wavelength that

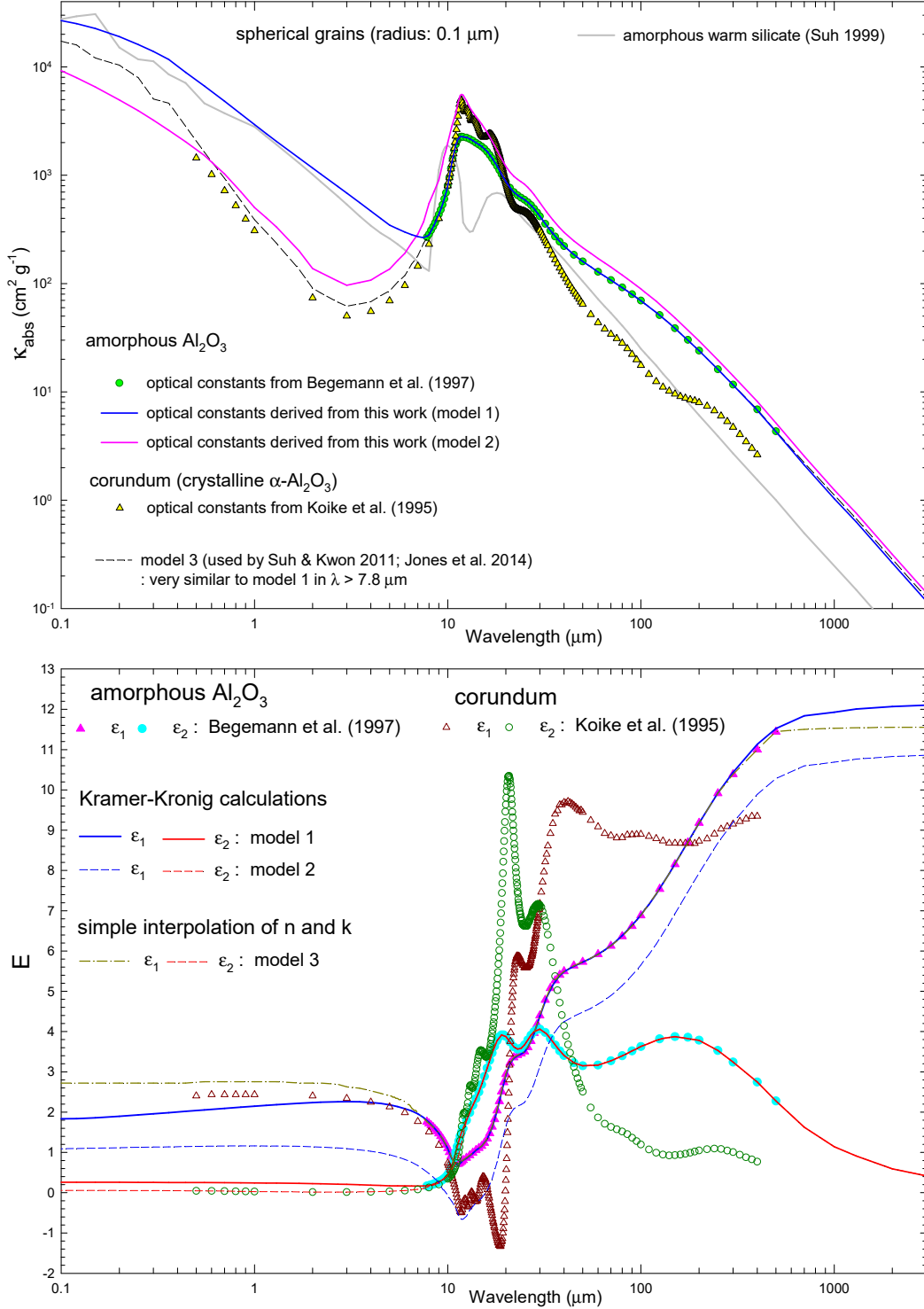


Figure 1. Opacity functions and indices of refraction for alumina dust.

sets the scale of the dust optical depth (τ_{10}). For the central star, we assume that the luminosity is $10^4 L_{\odot}$ for all models. We assume that the stellar blackbody temperature is 2500–3000 K.

For dust opacity, we use a simple mixture of silicate and alumina (10–40% by number) dust grains as well as pure silicates. For silicate dust, we use the optical

constants of warm and cold silicate grains derived by Suh (1999). We use the warm silicate dust for LMOA stars (models with $\tau_{10} \leq 3$) and the cold silicate dust for HMOA stars (models with $\tau_{10} > 3$). For alumina dust, we use the optical constants of amorphous alumina derived from this work (model 1; see section 2.2) based on the laboratory data from Be97. We assume that all

dust grains are spherical with a uniform radius of $0.1 \mu\text{m}$.

3.1. Typical model SEDs

The upper panel of Figure 2 shows the typical model SEDs for LMOA stars. The lower panel of Figure 2 shows the typical model SEDs for HMOA stars. They show the theoretical model SEDs using a simple mixture of silicate and alumina dust as well as pure silicates. We assume that the stellar blackbody temperature is 2500 K for LMOA stars and 2000 K for HMOA stars. The dust condensation temperature (T_c) is assumed to be 1000 K.

3.2. Comparison of the model SEDs with the observations

In Figures 3 and 4, we compare the observed SEDs with the theoretical model SEDs for the two LMOA stars (omi Cet and Z Cyg) and two HMOA stars (OH 127.8+0.0 and OH 21.5+0.5). For the objects, the spectral data from the Infrared Space Observatory (ISO) and Infrared Astronomical Satellite (IRAS) Low Resolution Spectrograph (LRS; $\lambda = 8\text{--}22 \mu\text{m}$) are used. We use the ISO data from the Short Wavelength Spectrometer (SWS; $\lambda = 2.4\text{--}45.4 \mu\text{m}$) and Long Wavelength Spectrometer (LWS; $\lambda = 43\text{--}197 \mu\text{m}$). We also use the photometric data from the IRAS Point Source Catalog (PSC) and AKARI (Murakami et al. 2007).

For LMOA stars, the stellar blackbody temperature is assumed to be 2500 K and 2650 for omi Cet and Z Cyg, respectively. The dust condensation temperature (T_c) is assumed to be 654 K and 463 K for omi Cet and Z Cyg, respectively. Suh (2004) pointed out that T_c looks to be low (400–800 K) for LMOA stars with thin dust envelopes.

For both LMOA stars, a mixture of amorphous alumina with silicate dust grains produces different model SEDs compared to the model SEDs produced by pure silicate dust in $\lambda = 8\text{--}20 \mu\text{m}$. The mixture of amorphous alumina dust looks to reproduce the observed SEDs better in $\lambda = 11\text{--}15 \mu\text{m}$. Other important dust species such as MgFeO series may need to be considered to make a better fit. The dust grains of MgFeO series produce single peaks in $\lambda = 15\text{--}22 \mu\text{m}$ (Henning et al. 1995).

In Figure 4, the observed SEDs are compared with the theoretical model SEDs for HMOA stars. For the two HMOA stars, we find that the amorphous alumina dust is not useful to reproduce the observed SEDs. For both objects, the stellar blackbody temperature is assumed to be 2000 K and T_c is assumed to be 1000 K.

4. IR 2CDs FOR O-RICH AGB STARS

IR 2CDs are useful to characterize the dust envelopes around AGB stars and post-AGB stars (e.g., Suh 2015). Suh & Kwon (2011) presented a list of AGB stars for 3003 O-rich stars in our Galaxy and Kwon & Suh (2012) presented a revised sample of 3373 O-rich AGB stars.

For the sample O-rich AGB stars, we obtain photometric data in three bands (12, 25, and $60 \mu\text{m}$) by using version 2.1 of the IRAS PSC. We also use the AKARI PSC data in two bands (9 and $18 \mu\text{m}$) obtained by the infrared camera, Two Micron All Sky Survey (2MASS; Cutri et al. 2003) data in K_s ($2.159 \mu\text{m}$) band, and Midcourse Space Experiment (MSX; Egan et al. 2003) data in four broad bands centered at 8.28, 12.13, 14.65, and $21.34 \mu\text{m}$. We cross-identify the AKARI, 2MASS, and MSX sources by finding the nearest one from the IRAS PSC position.

The color index is defined by

$$M_{\lambda_1} - M_{\lambda_2} = 2.5 \log_{10} \frac{F_{\lambda_2}/ZMC_{\lambda_2}}{F_{\lambda_1}/ZMC_{\lambda_1}} \quad (2)$$

where ZMC_{λ_i} means the zero magnitude calibration at given wavelength (λ_i) (see Suh & Kwon 2011 for details). We use only those objects with good quality data at any wavelength.

Figures 5 and 6 show the IR 2CDs for the 3373 O-rich AGB stars compared with theoretical models. The small symbols are observational data and the lines with large symbols are theoretical model calculations for a range in dust-shell optical depth. We explain the theoretical models in Section 4.1. Generally, the stars in the upper-right region on the 2CDs have thick dust shells with large optical depths.

4.1. Theoretical Models for the 2CDs

We use the radiative transfer model for the dust shells around O-rich AGB stars as explained in section 3. We perform the model calculations for eleven optical depths ($\tau_{10} = 0.005, 0.01, 0.05, 0.1, 0.5, 1, 3, 7, 15, 30,$ and 40). We assume that the stellar blackbody temperature is 2500 K for $\tau_{10} \leq 3$ and 2000 K for $\tau_{10} > 3$. The dust condensation temperature (T_c) is assumed to be 500 K and 1000 K.

We use the warm silicate dust for LMOA stars (7 models with $\tau_{10} \leq 3$) and cold silicate dust for HMOA stars (4 models with $\tau_{10} > 3$). We also show the models using a simple mixture of silicate and alumina (20–40%) dust. Generally, the theoretical model points in the upper-right region on a 2CD have large dust optical depths (or thick dust envelopes).

4.2. Comparison on 2CDs

Figures 5 and 6 show the IRAS, IRAS-NIR, MSX, IRAS-AKARI 2CDs for O-rich AGB stars compared with the theoretical models. LMOA stars are located in the lower-left region and HMOA stars are located in the upper-right region (lower-right region for the MSX 2CD) in all 2CDs. Generally, we find that the basic theoretical model tracks roughly coincide with the densely populated observed points.

The theoretical model tracks are shown for dust condensation temperatures (T_c) of 500 K and 1000 K. Suh (2004) pointed out that a lower T_c ($T_c < 1000$ K) is required for LMOA stars with thin dust envelopes. Generally, we find that the models with a higher T_c (1000

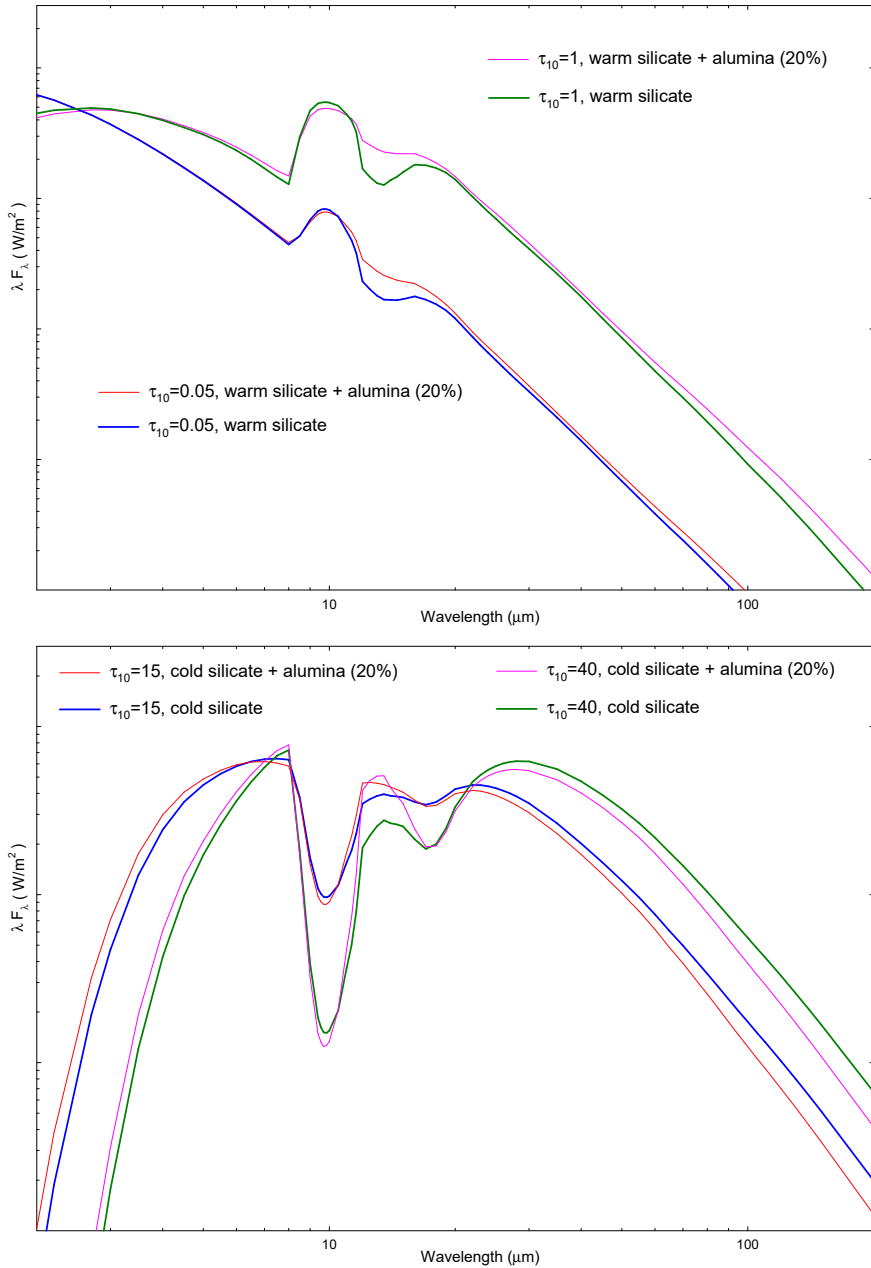


Figure 2. Theoretical model SEDs for O-rich AGB stars.

K) reproduce the observations of HMOA stars better while the models with a lower T_c (500 K) reproduce the observations of LMOA stars better for most 2CDs.

The shape of the 10 μm feature of O-rich AGB stars, which is mainly produced by silicate, can be modified by addition of the alumina dust. Because amorphous alumina dust produces a single peak at 11.8 μm , the AKARI, IRAS, and MSX fluxes at 9, 8.28, 12, and 14.65 μm would be easily affected by the alumina dust. The dust grains of MgFeO series (Henning et al. 1995) produce single peaks in λ 15–22 μm which could be responsible for the MSX flux at 14.65 and 21.34 μm . The models with pure silicate dust opacity do not make satisfactory fits for some 2CDs possibly because of the pres-

ence of alumina and MgFeO series dust.

The upper panel of Figure 5 plots AGB stars in an IRAS 2CD using [25]–[60] versus [12]–[25]. The model lines using a mixture of alumina are different from those using pure silicate because the IRAS flux at 12 μm is affected by addition of alumina dust. For HMOA stars, the alumina models are not useful because they produce exceedingly large [12]–[25] colors because the alumina dust modifies the 10 μm silicate absorption feature resulting in the smaller flux at 12 μm .

The lower panel of Figure 5 shows an IRAS-NIR 2CD using [12]–[25] versus K –[12]. For LMOA stars, the alumina models are very useful because they produce smaller [12]–[25] colors because the alumina dust mod-

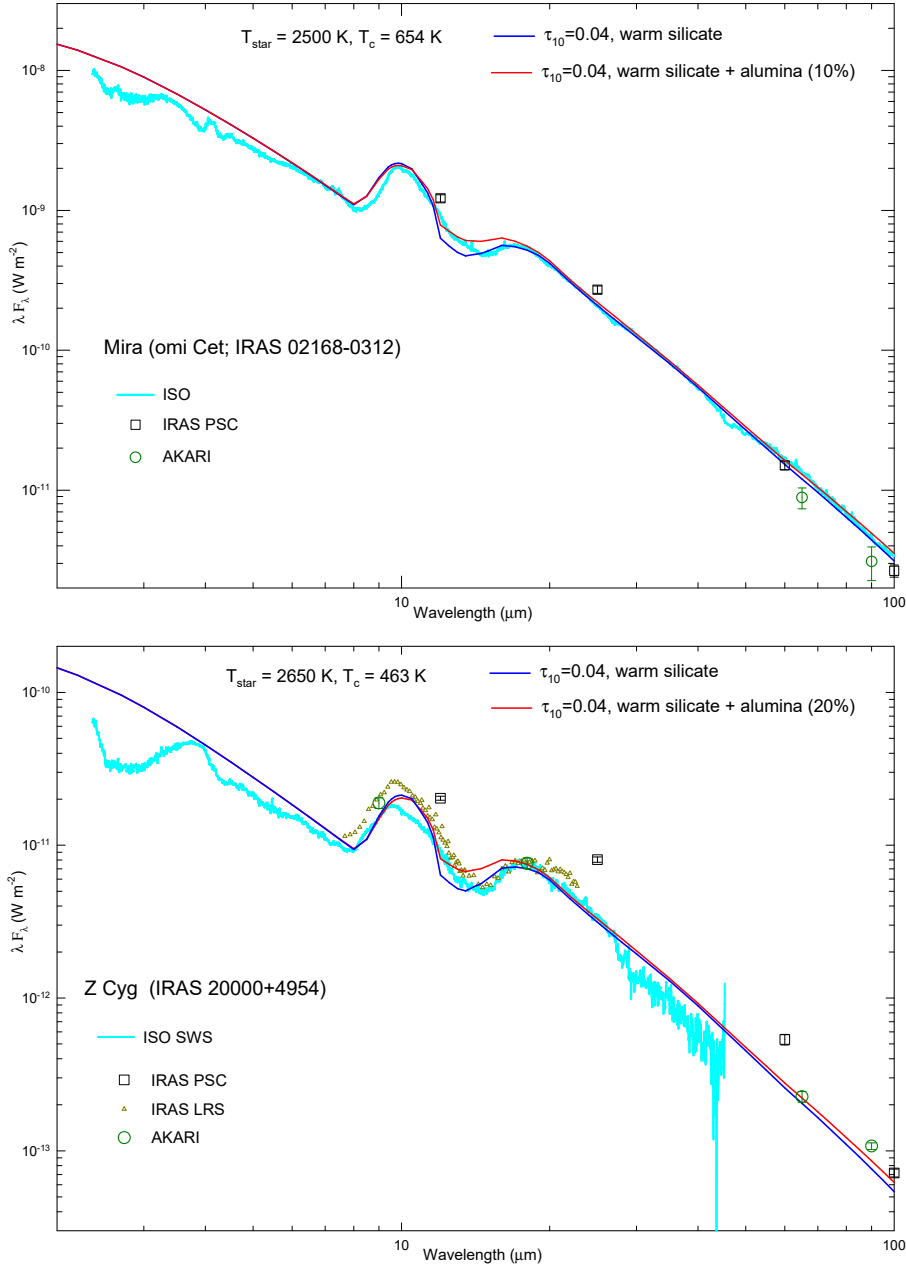


Figure 3. Model SEDs compared with the observed SEDs for LMOA stars.

ifies the 10 μ m silicate emission feature resulting in the larger flux at 12 μ m. The alumina models can easily reproduce the LMOA stars in the lower-left region of the 2CD.

The upper panel of Figure 6 shows a MSX 2CD using [8.28]–[14.65] versus [14.65]–[21.34]. The MSX fluxes at 14.65 μ m are affected by the alumina dust. The alumina models can reproduce the LMOA stars in the upper-left region because the [8.28]–[14.65] colors become redder (or larger) due to the alumina dust, which produces more emission at 14.65 μ m (see the upper panel of Figure 2).

On the MSX 2CD, the theoretical model points for very large dust optical depths are located in lower-

right region, unlike other 2CDs. This is because the [8.28]–[14.65] colors become bluer (or smaller) for large dust optical depths due to the deep silicate absorption feature at 18 μ m, which lower the flux at 14.65 μ m relative to the flux at 8.28 μ m (see the lower panel of Figure 2). The objects in the upper-right region could be post-AGB stars (see Suh 2015).

The lower panel of Figure 6 shows an AKARI-IRAS 2CD using [12]–[25] versus [9]–[25]. This 2CD shows the largest deviations of the theoretical models from the observations because of the AKARI flux at 9 μ m. The similar effects were noticed in Suh & Kwon (2011). The observed points in the lower-left region of the 2CD can be reproduced by the theoretical models using the larger

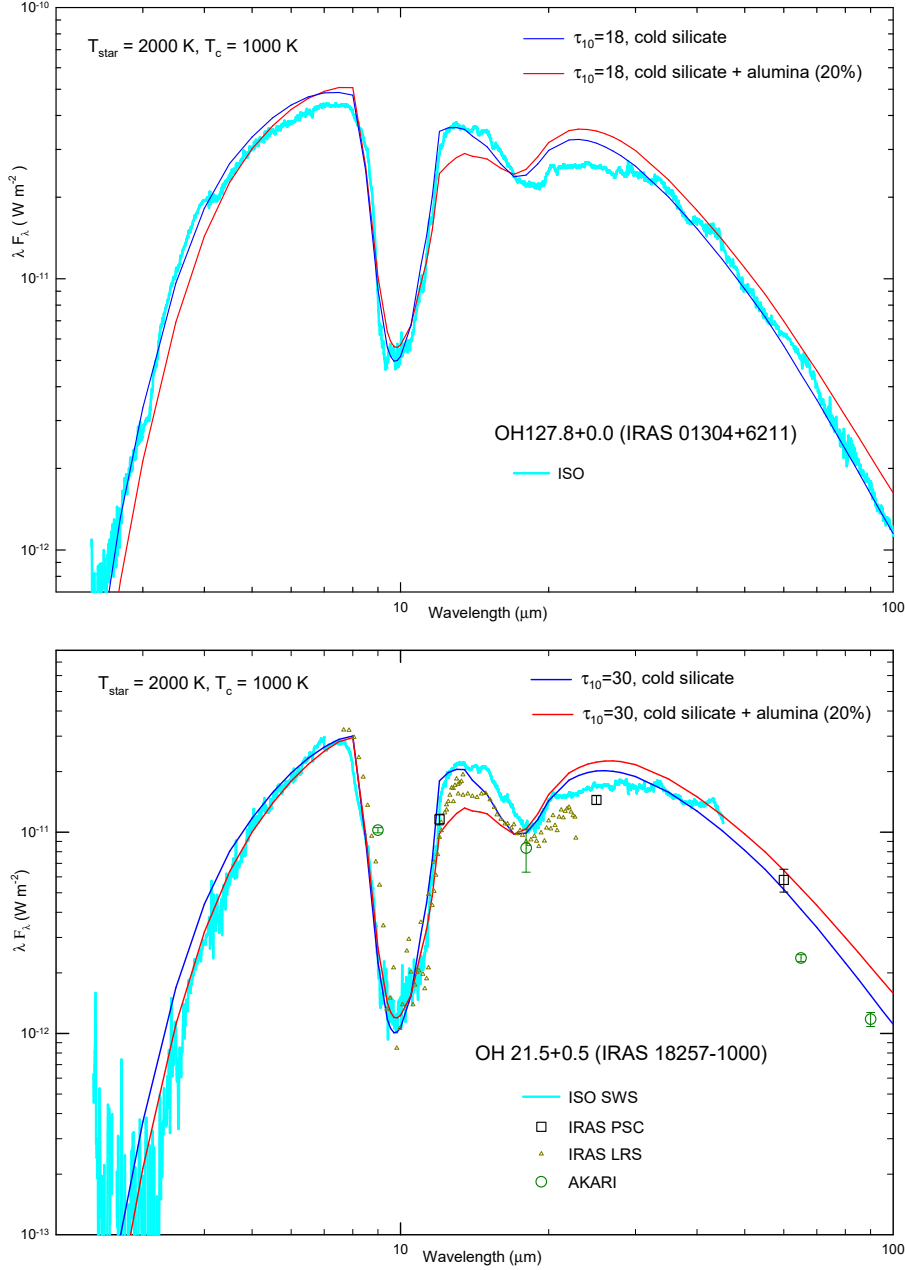


Figure 4. Model SEDs compared with the observed SEDs for HMOA stars.

alumina contents (40-50 %), compared with other 2CDs.

For all IR 2CDs, we find that the amorphous alumina dust is useful only for LMOA stars with thin dust envelopes which show the silicate emission features at 10 and 18 μm .

5. SUMMARY

In this work, we have investigated optical properties of the amorphous alumina (Al_2O_3) dust grains in the envelopes around O-rich AGB stars, considering the laboratory measured optical data. We have derived the optical constants of the amorphous alumina dust in a wide wavelength range, which satisfy the Kramers-Kronig relation and reproduce the laboratory measured

data.

Amorphous alumina grains produce a single peak at 11.8 μm and influences the shape of the SED at around 10 μm . The shape of the 10 μm feature of O-rich AGB stars, which is mainly produced by silicate, can be modified by addition of the alumina dust. Using the opacity function of the alumina dust, we have compared the theoretical radiative transfer model results with the observed SEDs and observations on various IR 2CDs for a large sample O-rich AGB stars.

Even though it is difficult to suggest the exact content of amorphous alumina for O-rich AGB stars because dust species other than alumina can also produce similar features in the wavelength range 8-15 μm , we have

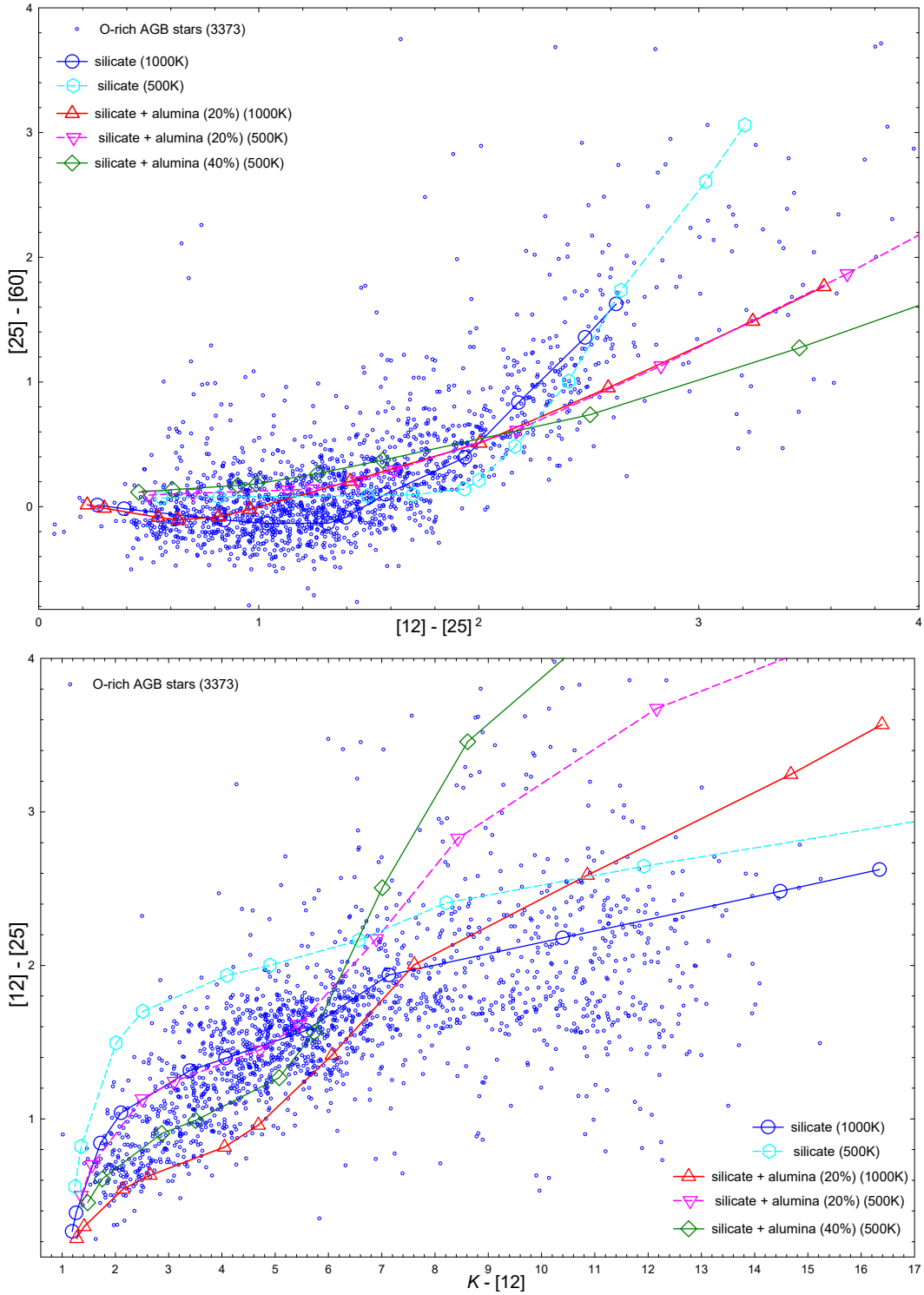


Figure 5. IR 2CDs for O-rich AGB stars compared with theoretical dust shell models (from left to right: $\tau_{10} = 0.005, 0.01, 0.05, 0.1, 0.5, 1, 3, 7, 15, 30,$ and 40).

found a general trend for a large sample of the stars on 2CDs. Comparing the theoretical models with the observations on various IR 2CDs, we have found that the amorphous alumina dust (about 10-40 %) mixed with amorphous silicate can reproduce much more observed points for LMOA stars, which have thin dust

envelopes. Because the alumina dust is not useful for HMOA stars, we expect that the relative alumina abundance for LMOA stars is higher than the abundance for HMOA stars with thick dust envelopes.

We expect that the optical constants for amorphous alumina derived in this work would be

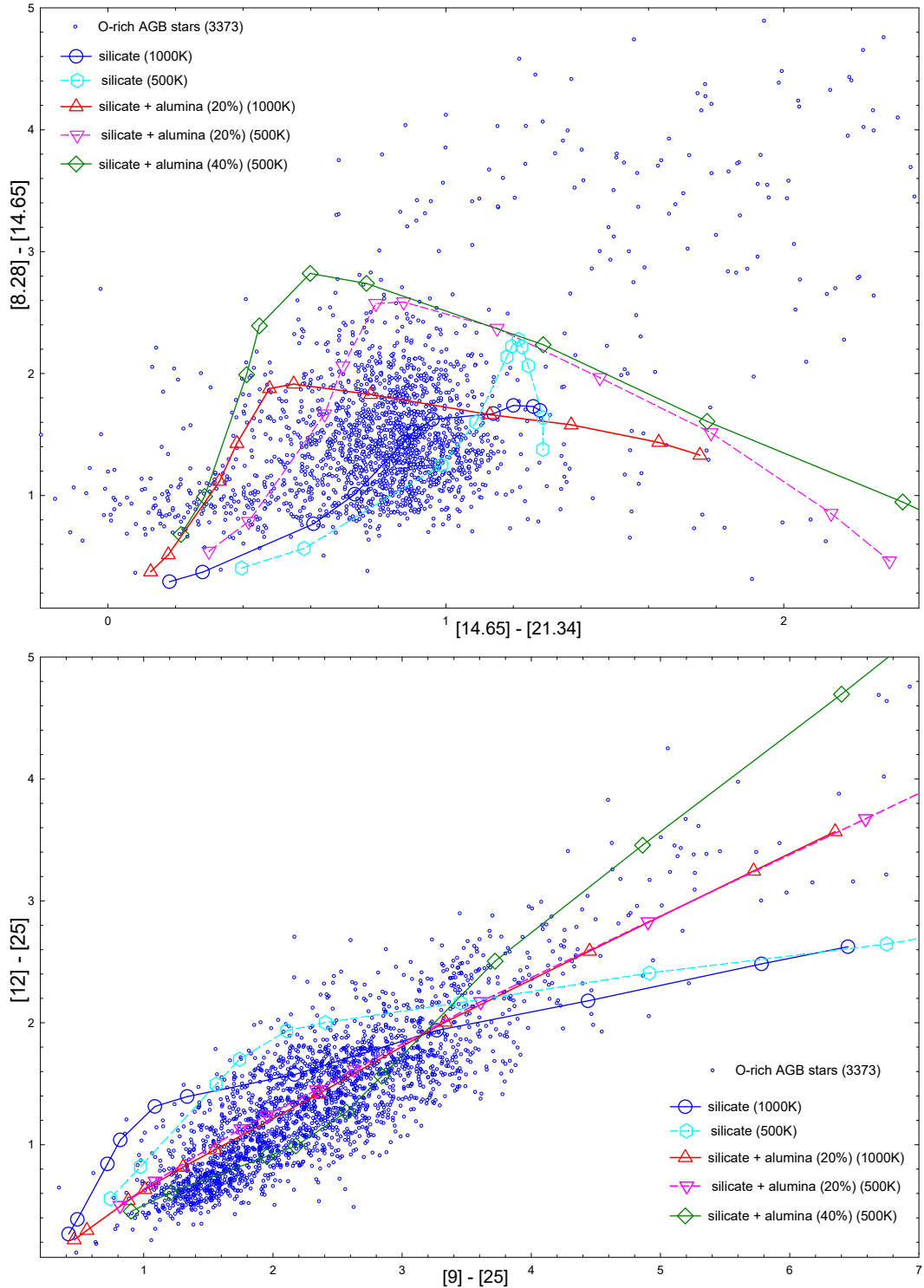


Figure 6. IR 2CDs for O-rich AGB stars compared with theoretical dust shell models (from left to right: $\tau_{10} = 0.005, 0.01, 0.05, 0.1, 0.5, 1, 3, 7, 15, 30,$ and 40).

useful for further studies on dust around AGB and post-AGB stars. The optical constants for the amorphous alumina derived in this work will be accessible through the author's web site: <http://web.chungbuk.ac.kr/~kwsuh/d-opt.htm>.

ACKNOWLEDGMENTS

This research was supported by Basic Science Research Program through the National Research Foundation of Korea (NRF) funded by the Ministry of Science, ICT & Future Planning (NRF-2013R1A1A2057841). This work was supported by the intramural research grant of

Chungbuk National University in 2015.

REFERENCES

- Begemann, B., Dorschner, J., Henning, T., et al. 1997, Aluminum Oxide and the Opacity of Oxygen-rich Circumstellar Dust in the 12-17 Micron Range, *ApJ*, 476, 199
- Bohren C. F., & Huffman D. R. 1983, *Absorption and Scattering of Light by Small Particles* (New York: Wiley)
- Cutri, R. M., Skrutskie, M. F., Van Dyk, S., et al. 2003, VizieR Online Data Catalog: 2MASS All-Sky Catalog of Point Sources
- Egan, M. P., Price, S. D., Kraemer, K. E., et al. 2003, VizieR Online Data Catalog: MSX6C Infrared Point Source Catalog
- Egan, M. P., & Sloan, G. C. 2001, The Physical Basis for the Silicate Dust Sequence, *ApJ*, 558, 165
- Henning, Th., Begemann, B., Mutschke, H., & Dorschner J., 1995, Optical Properties of Oxide Dust grains, *A&AS*, 112, 143
- Ivezić, A., & Elitzur, M. 1997, Self-Similarity and Scaling Behaviour of Infrared Emission from Radiatively Heated Dust - I. Theory, *MNRAS*, 287, 799
- Jones, O. C., Kemper, F., Srinivasan, S., et al. 2014, Modelling the Alumina Abundance of Oxygen-Rich Evolved Stars in the Large Magellanic Cloud, *MNRAS*, 440, 631
- Jones, T. W., & Merrill, K. M. 1976, Model Dust Envelopes around Late-type Stars, *ApJ*, 209, 509
- Justtanont, K., Olofsson, G., Dijkstra, C., & Meyer, A. W. 2006, Near-infrared observations of water-ice in OH/IR stars, *A&A*, 450, 1051
- Koike C., Kaito C., Yamamoto T., Shibai H., Kimura S., Suto H., 1995, Extinction Spectra of Corundum in the Wavelengths from UV to FIR, *Icarus*, 114, 203
- Kwon, Y.-J., & Suh, K.-W. 2012, Properties of OH, SiO, and H₂O Maser Emission in O-Rich AGB Stars, *JKAS*, 45, 139
- Markwick-Kemper, F., Gallagher, S. C., Hines, D. C., & Bouwman, J., 2009, Dust in the Wind: Crystalline Silicates, Corundum, and Periclase in PG 2112+059, *ApJ*, 668, L107
- Murakami, H., Baba, H., Barthel, P., et al. 2007, The Infrared Astronomical Mission AKARI, *PASJ*, 59, 369
- Sloan, G. C.; Price, S. D. 1998, The Infrared Spectral Classification of Oxygen-rich Dust Shells, *ApJS*, 119, 141S
- Speck, A. K., Barlow, M. J., Sylvester, R. J., Hofmeister, A. M. 2000, Dust features in the 10 μ m infrared spectra of oxygen-rich evolved stars, *A&AS*, 146, 437
- Suh, K.-W. 1999, Optical Properties of the Silicate Dust Grains in the Envelopes around Asymptotic Giant Branch Stars, *MNRAS*, 304, 389
- Suh, K.-W. 2004, Pulsation Phase-Dependent Dust Shell Models for Oxygen-Rich Asymptotic Giant Branch Stars, *ApJ*, 615, 485
- Suh, K.-W. 2015, Infrared Two-Color Diagrams for AGB stars, post-AGB stars, and Planetary Nebulae, *ApJ*, 808, 165
- Suh, K.-W., & Kwon, Y.-J. 2011, Infrared Two-Colour Diagrams for AGB Stars Using AKARI, MSX, IRAS and Near-Infrared Data, *MNRAS*, 417, 3047
- Suh, K.-W., & Kwon, Y.-J. 2013, Water Ice in High Mass-loss Rate OH/IR Stars, *ApJ*, 762, 113
- Zeidler, S., Posch, Th., & Mutschke, H. 2013, Optical constants of refractory oxides at high temperatures. Mid-infrared properties of corundum, spinel, and alpha-quartz, potential carriers of the 13 μ m feature, *A&A*, 553, 81